Integrating Landsat Imageries and Digital Elevation Models to Infer Water Level Change in Hoover Dam

Kuo-Hsin Tseng, C. K. Shum, Jin-Woo Kim, Xianwei Wang, Kefeng Zhu, and Xiao Cheng

***Abstract*—The Thematic Mapper onboard Landsat 4, 5, and Enhanced Thematic Mapper Plus (TM/ETM+) onboard Landsat 7 have frequency bands (green and SWIR) to effectively measure water body extents and their changes via the Modified Normalized Difference Water Index (MNDWI). Here, we developed a technique, called the thematic imagery-altimetry system (TIAS), to infer the vertical water changes from MNDWI horizontal water extent changes by integrating long-term TM/ETM+ imageries with available digital elevation models (DEMs). The result is a technique to quantify water level changes of natural or artificial water bodies over two decades. Several DEMs were used to compute intersects with TM/ETM+ water extent time series to evaluate the robustness of the technique. These DEMs include: the Advanced Spaceborne Thermal Emission and Reflection Radiometer Global Digital Elevation Map version 2 (ASTER-GDEM2, at 1 arcsec resolution), the Shuttle Radar Topography Mission version 2 (SRTM C-band at 1 arcsec), and the Global Multiresolution Terrain Elevation Data (GMTED2010 at 7.5 arcsec). We demonstrated our technique near Hoover Dam (HD) in Lake Mead to quantify its respective decadal water level changes. The dammed water had experienced extraordinary level variation in the past 20 years due to natural decline from intake or artificial impoundments. The discrepancy of the HD water level changes from an analysis of 32-year (1984–2015) time series, including 584 Landsat scenes, using the GMTED2010 DEM, has a RMSE reached 0.85 ± 0.63 m (91% of data) as compared with *in situ* stage record.**

***Index Terms*—Inland water altimetry, lake level, remote sensing, shoreline detection.**

Manuscript received July 28, 2015; revised October 07, 2015; accepted November 4, 2015. This work was supported in part by the Ministry of Science and Technology (MOST), Taiwan, under project 104-2119-M-008-005-MY2 and 104-2221-E-008-099-MY3, in part by the National Central University New Faculty Research Award. The U.S. component of the research is supported in part by the National Geospatial-Intelligence Agency under NGA/NURI HM1582-10-1-0019, and by NASA's Geodetic Imaging Program (NNX12AQ07G). The ICESat component was supported in part by the China's National Key Science Program for Global Change Research under Grant 2012CB957704, in part by the Fundamental Research Fund for the Central University, the Center for Global Sea Level Change (CSLC) of NYU Abu Dhabi under Grant G1204, and in part by the Open Fund of State Key Laboratory of Remote Sensing Science under Grant OFSLRSS201414.

K.-H. Tseng is with the Center for Space and Remote Sensing Research, National Central University, Taoyuan 32001, Taiwan, and also with the Institute of Hydrological and Oceanic Sciences, National Central University, Taoyuan 32001, Taiwan (e-mail: khtseng@csrsr.ncu.edu.tw).

C. K. Shum is with the State Key Laboratory of Geodesy and Earth's Dynamics, Institute of Geodesy and Geophysics, Chinese Academy of Sciences, Wuhan 430077, China, and also with the Division of Geodetic Science, School of Earth Sciences, Ohio State University, Columbus, OH 43210 USA (e-mail: ckshum@osu.edu).

K. Zhu is with the Division of Geodetic Science, School of Earth Sciences, Ohio State University, Columbus, OH 43210 USA (e-mail: zhu.218@osu.edu).

J.-W. Kim is with the School of Earth Sciences, Southern Methodist University, Dallas, TX 75275 USA (e-mail: jinwook@smu.edu).

X. Wang is with the State Key Laboratory of Remote Sensing Science, Institute of Remote Sensing Applications, Chinese Academy of Sciences, and Beijing Normal University, Beijing 100875, China, and also with the Center for Global Sea Level Change, New York University Abu Dhabi, Abu Dhabi 129188, UAE (e-mail: wangxianwei0304@163.com).

X. Cheng is with the College of Global Change and Earth System Science, Beijing Normal University, Beijing 100875, China (e-mail: xcheng@bnu.edu.cn).

Color versions of one or more of the figures in this paper are available online at http://ieeexplore.ieee.org.

Digital Object Identifier 10.1109/JSTARS.2015.2500599

I. Introduction

CHANGES in water surface height (WSH) over time for inland water bodies are critical information for freshwater studies and water resource management. Spaceborne observation has thus become a promising tool for large-scale observation that supports locally incomplete infrastructure, such as gauge stations [1]–[3]. Owing to the advance in satellite altimetry and postprocessing techniques such as radar waveform retracking [4]–[6], monitoring large ($>100\,\mathrm{km}^2$) inland water bodies has been made possible in the past two decades by data from multiple satellite radar altimetry missions [7] or data from laser altimetry mission, such as ICESat [8].

In principle, the distance between satellite and its nadir point on the Earth could be determined by measuring the two-way travel time between emission and reception of radar pulses (or photons in laser pulses), assuming that they travel in the speed of light in vacuum. After several corrections for distance due to inhomogeneous media (e.g., troposphere and ionosphere) and tidal effects, the ellipsoidal height of the nadir point can thus be approximated by subtracting the satellite-surface distance from the height of satellite itself. Following to these corrections, the radar waveform retracking fine-tunes the telemetered range from radar echoes sampled in time, or equivalent in distance. Tracing the shape of a waveform, especially the position and slope of leading/trailing edge with respect to a nominal location in waveform gates, provides information about surface roughness and tilt of the plane within the radar footprint.

However, these measurements obtained from repeat-orbiting satellites are strictly confined to a predefined ground-track grid and a periodical sampling based on orbit characteristics. For example, the Environmental Satellite (Envisat) launched by the European Space Agency (ESA) in 2002 had a cross-track interval $\sim$80 km at the Equator and 35-day revisit period, which shared the same orbital elements with preceding ERS-1/-2 missions back to the 1990s. Another example is NASA/CNES's TOPEX/Poseidon (T/P), Jason-1, and OSTM/Jason-2 series that has a coarser along-track spacing at the Equator ($\sim$315 km) and a shortened revisit period of $\sim$10 days [9], [10]. In addition, the ICESat laser altimetry working in campaign mode

in a period of 2003–2010 had only 2–3 revisits per year [11], despite its dense ground-track separation of about 7 km. Although the altimetry satellite such as T/P and Jason-1 was built intentionally for open-ocean or sea ice studies, along with some following missions, for instance, Jason-2, Envisat, ICESat, and SARAL/AltiKa, they have contributed enormously to the terrestrial hydrology [8], [12]–[20] and many other continental freshwater applications [5], [12], [21]–[23]. However, the demand at some particular locations is sometimes totally unattainable while the target area falls between parallel ground-tracks without any possible fly-bys. Meanwhile, the footprint of the conventional pulse-limited radar altimeter usually varies between 3 and 7 km in radius depending on the surface roughness for terrestrial measurements. The footprint partially covering land may encounter a serious land contamination in echoes and usually needs further waveform editing [24]–[26], especially for water surface less than 1 km wide [27]. Therefore, an alternative method using swath imaging is considered to complement spatial/temporal gaps bypassed by these pulse-limited radar or laser altimetry satellites. To a greater extent, this alternative method is expected to have a broader coverage of terrestrial area and seamless mission time span, which supports operational and long-term observations of WSH variations.

Considering the altimetric satellite that is scheduled for launch, the Surface Water Ocean Topography (SWOT) mission [1], [28] carrying the Ka-band radar interferometer (KaRIn) may be the only candidate to fulfill this anticipation. For example, Frappart *et al.* [29] presents the signature on surface water of the extreme drought that affected the Amazon basin in 2005 in a SWOT perspective. Other missions, such as SARAL/AltiKa (launched in February 2013), Sentinel-3 (scheduled for launch in late 2015), Jason-3 (2015), and Jason-CS (Continuity of Service, 2017) will perhaps follow similar orbits and equip nadir-looking radar or delay-Doppler [30] altimeters as their predecessors. Hence, before the expected launch of SWOT in 2020, an alternative method is needed to study the inland waters variation from historical satellite records. Previous works have demonstrated the potential of combining nadir altimetry measurements with various types of satellites images to quantify water volume stored in lakes, floodplains and large river basins, such as using SAR [31], multispectral [32], [33], and multisatellite observations [29].

In the last few years, numerous studies have been dedicated to the computation of water surface area (WSA) using remote sensing (RS) imagery and compared the results to various water level measurements [34]–[38], such as *in situ* gauge data. In fact, the WSH of water body itself can be approximated by monitoring the WSA expansion moving along the contour of an accurate reference elevation, as long as the side slope of a lake is not vertical. And the WSH can be directly validated by the gauge or altimetry measurements, if they were existed. However, the possibility of conversion between WSA and WSH had been poorly investigated in the literatures, due primarily to the high cost of very high-resolution optical imagery and unavailability of good topography references. Pietroniro *et al.* [39] demonstrated this concept using Landsat Multispectral Scanner (MSS) and Thematic Mapper (TM) images, coupled with GPS-derived digital elevation model (DEM) at the Peace-Athabasca Delta (PAD) in Canada. They included 8 Landsat snapshots in 16 years and obtained water level in <20 cm accuracy compared with hydraulic model over the very low-relief PAD floodplain. Xu *et al.* [40] used QuickBird-2 submeter resolution imagery to estimate river discharge along Yangtze River. However, they only used 5 images in multiple locations and relied on a look-up table for river width-stage conversion. Andreoli *et al.* [41] showed an integration of Envisat ASAR/MERIS images with SRTM-C at Poyang Lake, China. In their study, the monitor of lake level in the flat Poyang Lake had an average error at 1.26 ± 1.83 m. Cai *et al.* [42] analyzed MODIS imageries and construct a area-level relationship also in Poyang Lake. They obtained high correlation between water area and water level at R^2 equal 0.61–0.98 by multiple regression models.

Due to the rising accessibility of several high resolution DEMs released in the last couple of years, the operational and global-covering virtue of this approach becomes feasible as we could employ high quality DEMs as a reference to recover the WSH more accurately for practical usage. Therefore, we intend to build such an algorithm namely the thematic imagery-altimetry system (TIAS) that aims to recover WSH by using a conceptually different principle than conventional nadir-looking radar or laser altimetry instruments. An introduction of study area will be given in Section II. A general workflow of the TIAS will be given in Section III, followed by a detailed description of data products and computational methods in Section IV. Statistics and error sources of the TIAS measurements in Lake Mead are tabulated and discussed in Section V. Finally, Section VI concludes the major contribution and prospective works from this study.

II. Study Site

To demonstrate the feasibility of this proposed approach, we applied the TIAS and examined its WSH estimate capability at Hoover Dam (HD) in Lake Mead. The HD located 40 km southeast of Las Vegas formed Lake Mead across Nevada and Arizona, USA, which is the largest reservoir in the USA since 1930s. During 2000–2010, the water level of Lake Mead at HD fell nearly 40 m due to the shortage of its intake [33]. The lake level dropped to 329.78 m above mean sea level, because of a reduction of flow along Colorado River from another giant reservoir upstream, the Glen Canyon Dam. After a short rebound during 2010–2013, the water level in Lake Mead kept hitting lowest level in all-time record since 2013, while the record in May 2015 is 328.14 m. The HD also incurred serious decrease in water volumes that are arguably subject to a secular trend in climate change [43], [44] and groundwater depletion [45]. In this study, the Boulder Basin, which is a part of western Lake Mead, was taken for investigation as specified in Fig. 1. The water area in the Boulder Basin is about $280\,\mathrm{km}^2$, with a shoreline length in some 450 km.

The HD in Lake Mead is not only socioeconomically important concerning its regional water storage/supply but also predominant in hydropower generation. However, relatively large

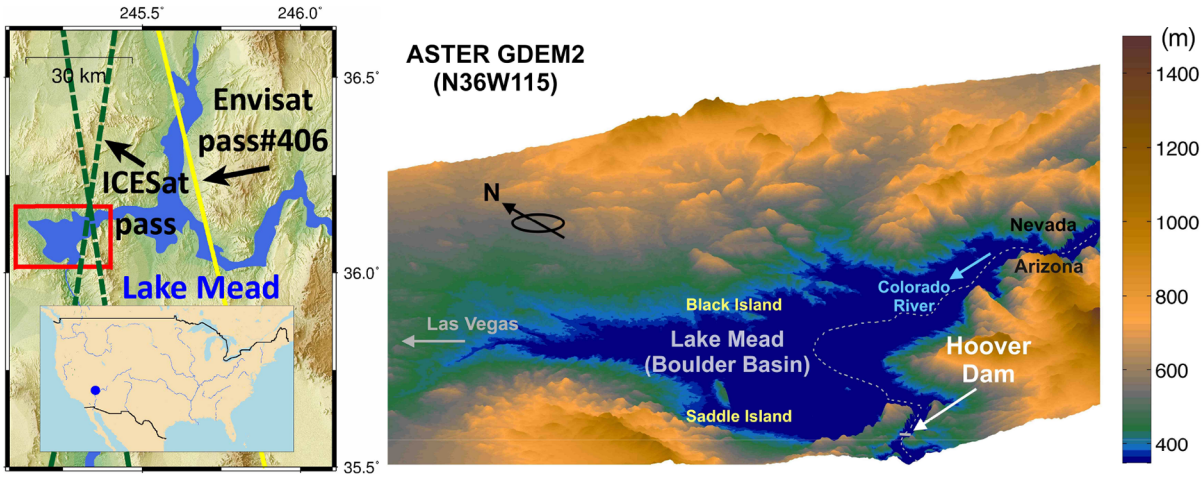

Fig. 1. Left panel denotes the geographical location of Lake Mead in the USA (blue dot in the inset) and the Boulder Basin aimed in this study (red box). Envisat pass #406 flying over the northern Overton Arm is denoted by yellow line. ICESat actual ground track near the Boulder Basin is denoted by green dashed line. The closest Jason-2 ground track falling east of the lake is not shown here. Right panel demonstrates a birdview of nearby terrain exemplified by ASTER GDEM2 in 30 m. The Boulder Basin covers a distance within ∼17 km from HD and a WSA stretches about 12 km in E–W and 10 km in N–S direction. We used addition masks to ensure WSA only covering upstream of the dam.

water areas of Lake Mead were infrequently monitored by radar altimeters, due primarily to the shape, terrain, and geographical locations that lack of ground tracks from a series of altimetry satellites. Although the surface area of entire lake is larger than 600 km^2, it has only covered by two Envisat passes with three crossovers ranging from 1.9 to 3.5 km. T/P and Jason-1/-2 series have no pass near this location (except for short-term extended/interlaced tracks). Therefore, an examination of the TIAS at this site is appropriate to demonstrate its comparable role in altimetric services. We perform an analysis of 32-year (1984–2015) water level study by collecting available Landsat imageries and *in situ* record, and compared with Envisat and ICESat data therein. The SARAL/AltiKa that follows Envisat is not included in current study.

III. Workflow of the TIAS

The TIAS has a three-tier architecture generally categorized in terms of data maturity levels, which include: 1) data collection; 2) preliminary estimate; and 3) Cal/Val sections as shown in Fig. 2. The steps from gathering data to converting WSA into WSH are also illustrated in Fig. 3 for visualization. In the beginning, the data collection part first gathers RS data and DEMs, and applies a preceding coregistration on both data sets. For DEM collection part, we utilized three popular products with spatial resolution ranging from 30 to 250 m, namely the Advanced Spaceborne Thermal Emission and Reflection Radiometer Global Digital Elevation Map version 2 (ASTER-GDEM2), Shuttle Radar Topography Mission C-band version 2 (SRTM-C), and Global Multiresolution Terrain Elevation Data (GMTED2010) (see details in Section IV-A). For RS imagery part, the TIAS algorithm employs both the TM carried by Landsat 4 and 5 and the Enhanced Thematic Mapper Plus (ETM+) onboard Landsat 7 to compute WSA. The Landsat series has nominally 30 m spatial resolution and 16-day revisit period. Since the grid size varies in each data

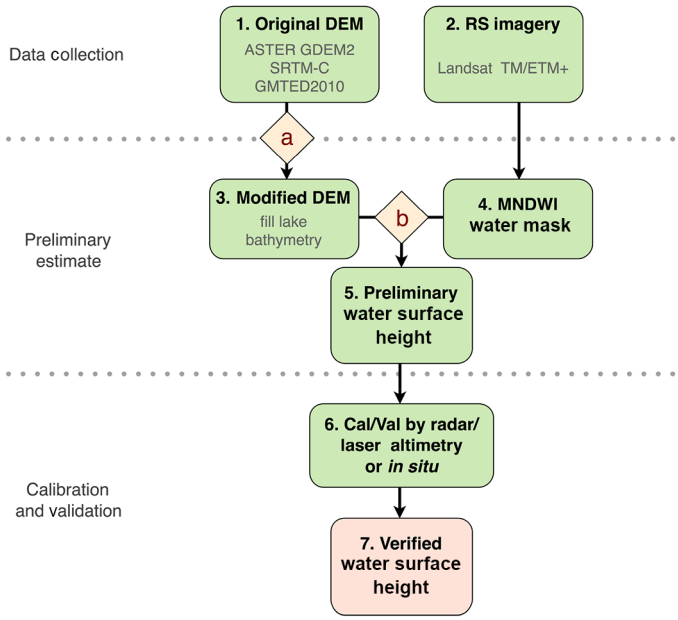

Fig. 2. Flowchart of the TIAS showing the process to estimate and verify WSH using RS imagery, DEMs, and other independent measurements. Two diamond boxes indicate technical processes required in the computation. (a) To fill the DEM water mask by a projection from nearby terrain. (b) To fit the distribution of height estimates by using the GEV fitting function. Step 6) is optional depending on the availability of *in situ* data or extra measurements.

source, it is necessary to align each pair of RS imagery and DEM to the same grid size via double-linear interpolation. We coregistered all datasets into 30 m grid and assume the geolocation error is ignorable.

After that, a modification for the DEM is needed because the raw data in these models cannot be directly used as their original forms—these DEMs have a constant elevation over lake area on the basis of a predefined water mask and the timing of composition [46]. Hence, a technical process denoted as diamond a in Figs. 2 and 3 is developed to replace the constant

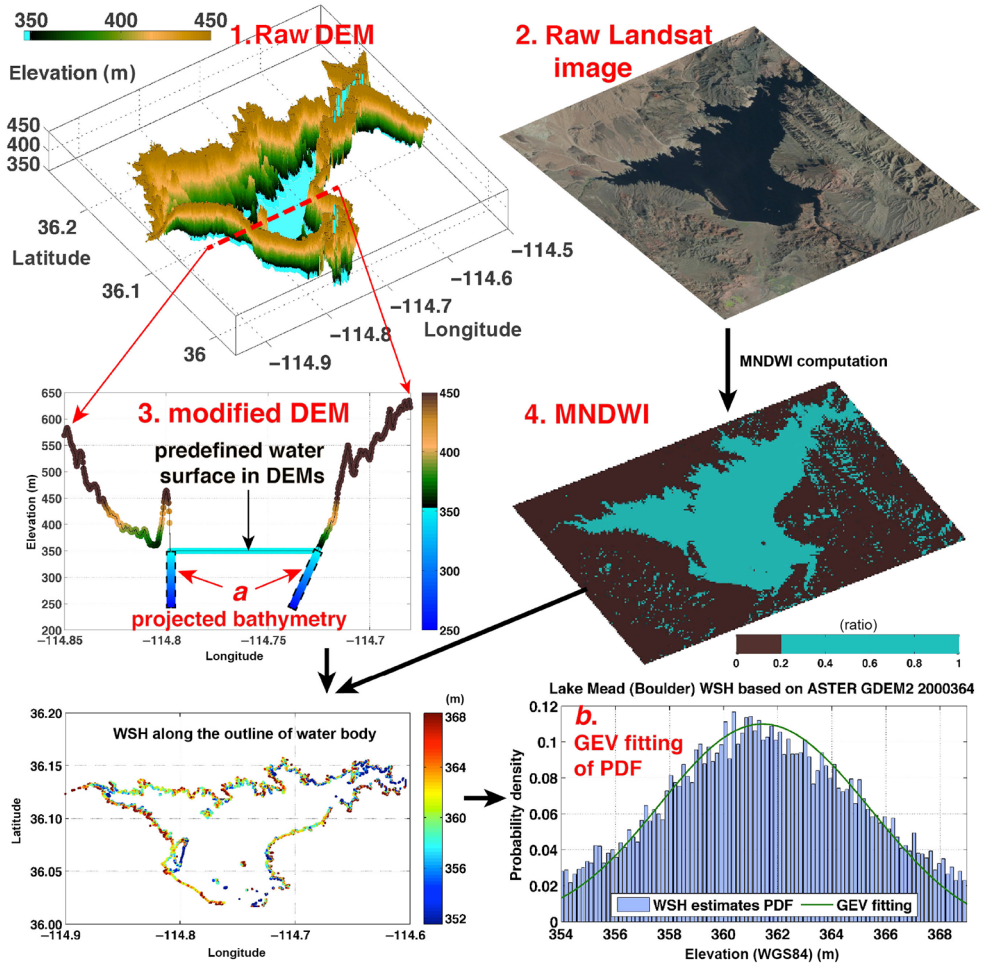

Fig. 3. Visualization of Steps 1–4) and technical processes a and b as marked in Fig. 2. Panel 1 is a 3-D elevation profile of Lake Mead near Boulder Basin. Panel 2 is the false-color composite image of a typical ETM+ scene (RGB: B5, B4, and B3). Panel 3 is a visualization of DEM modification process that extends the terrain inward of lake area to simulate the bathymetry near shore. Panel 4, a two color-coded plot, is an example of binarized MNDWI image that has been applied thresholding operation at a ratio equal 0.2. The bottom two panels are the scatter plot (left) and histogram of height distribution (right) for a typical ETM+ scene.

value in DEM over lake surface by a projection from the encompassing terrain. In other words, we assume that the side slope of a lake remains unchanged and can be extended toward the inundated area. As an example given in Fig. 3, a cross-section of lake bathymetry shown in panel 3 is profiled along the red dashed line in panel 1. The slope information from terrain in radial direction is gathered and extended downward to the lake bottom as denoted by a in panel 3. Although this projection of terrain may generate unreliable bathymetry close to the lake center since we assume that the depth of lake bottom is unlimited, based on our analysis, this approach remains effective as long as the WSH varies within few tens of meters at selected study site.

The Step 4) in the second part of TIAS consists of computing the Modified Normalized Difference Water Index (MNDWI) using Landsat TM/ETM+ imagery. The area whose MNDWI exceeding a certain threshold is marked as water and its boundary is then overlaid onto DEMs. If we assume that the equipotential surface of a particular water body has no surface gradient (i.e., geoid anomaly) or the anomaly is well known and can be corrected, the outline of such water body in steady state would match the contour of a DEM with respect to a vertical datum, such as the World Geodetic System 1984 (WGS84). The number of WSH "samples" is thus equal to the number of pixels along the shoreline, i.e., the total length of shoreline divided by the grid size of RS imagery (e.g., 30 m for Landsat). Ideally, there are a huge amount of samples with values centering to an exact ellipsoidal height, if we assume that the vertical and horizontal accuracy of the DEM is arbitrarily high and the grid size of RS imagery grid is infinite small. However, since the DEMs have various horizontal resolution (30–250 m) and vertical accuracy (7–30 m), while Landsat imagery also has limited spatial resolution (30 m) and inaccuracy in water mask determination, the collection of height estimates around the water body will practically form a probability distribution that allows us to compute the most likely WSH from fitting functions.

The second technical component denoted as diamond b in the flowchart is thus needed to find the best height estimate along the water body's outline. Each grid of shoreline has its corresponding height value from DEM after coregistration, and the value is considered to be the WSH at that pixel. The height samples gathered along the shoreline thus forms a histogram as also demonstrated in the bottom right of Fig. 3, panel b.

Since the WSH estimates collected along the shoreline may not be perfectly centering at just one value; instead, it has a spread across few meters depending on the quality of DEM and accuracy of shoreline determination. Therefore, finding the maximum likelihood estimate of WSH is a key component in this algorithm. In panel b, the histogram of WSH estimates is slightly different from a normal distribution consisting of unknown random noises. This probability distribution with a distinguishable peak may have uneven spread of shoulders (not shown here). For example, an inadvertent distortion of contour in DEM w.r.t. a vertical datum may cause a longer leg in either side of the distribution. Hence, we estimated the WSH by fitting the probability distribution of height estimates with the generalized extreme value (GEV) distribution that was developed to model the local maxima in a finite sequence [47]. Because the actual height of water surface is outstanding in the probability density function (pdf) and appears to be the outlying observation, regular normal distribution is poor in fitting the extreme value in pdf. Therefore, the GEV distribution that has been well known for modeling extreme events [48] corresponds well with requirement in this study.

The third part of the workflow includes the calibration/validation (Cal/Val) with other independent measurements having better accuracy that serve as groundtruth. In addition to the comparison with raw TIAS time series, we also provide a "de-outlier" version of time series for comparison. We used the moving average of TIAS time series itself to remove potential outliers in the measurements. More specifically, the difference between the TIAS WSH and three-point average was first computed, and then the outlying TIAS WSHs that exceeded 2-σ of the difference were discarded. The performance of using entire data set and after de-outlier process is both given in Section V. To validate the accuracy of TIAS results, we used monthly *in situ* measurements to validate TIAS WSH estimates, and also compared with ICESat GLAS laser altimetry and Envisat radar altimetry results. The quality indicators of WSH estimates include assessments of RMSE, correlation (R^2), and number of temporal points between measuring techniques. We also demonstrate an optional feedback mechanism showing a dynamic selection of MNDWI threshold by iterating a setting of 0.15, 0.2, and 0.25, in order to find the optimal threshold setting for certain image/DEM combination. The calibration step is only for lake that has other reference data and can be utilized to help TIAS accuracy.

IV. Data and Processing Technique in TIAS

A. Data Collection

1) Landsat TM/ETM+: The TM carried by Landsat 4 (1982–1993), Landsat 5 (1984–2012), and the ETM+ onboard Landsat 7 (1999–present) has provided a continuous services as land monitoring system from both photogrammetric and radiometric aspects. Both TM/ETM+ images can be browsed and downloaded via the U.S. Geological Survey (USGS) *EarthExplorer* interface (Available: http://earthexplorer.usgs.gov). After downloading the Level 1 product with separated bands in GeoTIFF format, the digital numbers (DNs) were then converted into the top-of-atmosphere (TOA) reflectance by means of appropriate calibration coefficients, including band-dependent rescaling factor, Sun azimuth, Earth–Sun distance, mean exoatmospheric solar irradiance ($ESUN_\lambda$), and the gain strength [49]. Moreover, following to the failure of the Scan Line Corrector (SLC), an instrument used to parallel each cross-track swath during the forward motion, in May 2003, the uncorrected scanning had resulted in a zigzag pattern of swath composite and caused stripe voids in each Landsat 7 ETM+ scene. Hence, approximately 22% of pixels in any given ETM+ scene remain unfilled. To address this problem, we applied a simple linear interpolation to fill void stripes in the computed MNDWI with binarized color-code, e.g., to set pixel whose MNDWI greater than 0.2 equal 1 and set pixel value equal 0 otherwise. On average, the SLC-off gaps at an interval approximately $\sim$1 km on the ground normally have 2–3 pixels in width at study site, which corresponds to a total $<$50 pixels at coastal region in one scene. Therefore, comparing to a great number of RS pixels along the shoreline, which is mostly $>14\,000$ pixels for HD (with a variation about 1500 pixels between high and low water level), the error due to the simplified manner of SLC-off correction is negligible. However, it should be emphasized that Boulder Basin lies in the center of the SLC-off Landsat scene (WRS Path: 39 Row: 35); therefore, the loss of pixels is minimal comparing with other lakes globally. For small lakes or lakes lying near the edge of a SLC-off scene, the treatment of data gaps should be more careful and a more sophisticated gap filling method should be applied. For this study, we first collected all TM/ETM+ images available over this region (1984–2015), and then rejected the ones with partial or full cloud-cover at study area by visual inspection. Finally, a number of 584 TM/ETM+ images (174 SLC-off mode) were used as an input in the TIAS computation.

2) Digital Elevation Models: Three DEMs exploited in this study are summarized in Table I. The higher resolution is SRTM-C and ASTER GDEM2 in 30 m [50], while the coarser one is GMTED2010 in $\sim$250 m [51]. Although GMTED2010, which uses SRTM digital terrain elevation data (void-filled) 30 m DEM as a major input at approximately 70% of its terrestrial coverage, the finest resolution of GMTED2010 has been reduced to $\sim$250 m to accommodate many other data sources in its global dataset [52]. For SRTM-C, we used SRTM1 V2 (30 m) in HD [53]. The SRTM X-SAR DEM had also been proposed and tested in the beginning of this study. However, since its meshed coverage only supports a fraction of lake surface in HD, it is thus excluded in the evaluation.

In addition, the last row of Table I remarks the elevation of water mask as the lower bound of WSH estimate while using raw DEM as an input. As mentioned before, the water mask in each DEM is identified while there is a polygon with constant value near the known location of water bodies. The GMTED2010 has the same water mask elevations as SRTM-C in HD, despite a 7-year transition between released dates. Also, the ASTER GDEM2 compiled after 2000 and released in 2009 has exclusively unveiled the WSH drop in HD during late 2000s, with a water mask elevation 22 m lower than others.

TABLE I
OVERVIEW OF DEM PRODUCTS USED IN THIS STUDY

Name	ASTER GDEM2	SRTM-C	GMTED2010
Generation and distribution	METI/NASA	NASA/USGS	USGS/NGA
Resolution	1 arcsec, approx. 30 m	1 (U.S. territory) and 3 (others) arcsec, approx. 30 m and 90 m	7.5–30 arcsec, approx. 250–1000 m
Altitude accuracy	7–14 m	10 m	26–30 m at 7.5 arcsec
Release year	2009	2003	2010
Data acquisition period	2000~ongoing	11-day STS-99 mission in February 2000	Multiple sources acquired in 2000–2010. Primarily SRTM, Canadian elevation data, Spot 5 reference3D, and data from ICESat.
Spatial coverage	83°N–83°S	60°N–56°S	83°N–56°S for most products
Coverage rate	100%	80% of earth landmass	100%
Area of missing data*	Areas with no ASTER data due to constant cloud cover (supplied by other DEM)	Topographically steep area (due to radar characteristics)	None
Instrument	ASTER	Space shuttle endeavour (NASA)	Multiple sources
Technique	Remote sensing (visible to thermal-infrared)	Interferometry C-Band	
Datum	World geodetic system 1984 (WGS 84) for horizontal and earth gravitational model 1996 (EGM96) geoid for vertical		
Water mask elevation at Lake Mead w.r.t. WGS84 in meter	350	372	372

* Except for bathymetry under waterbody.

3) Radar and Laser Altimetry: Launched in March 2002, Envisat operated by ESA was a near-polar-orbiting operational satellite with an inclination approximately 98.5°. Its sun-synchronous and exact-repeat orbital elements allowed the dual frequency radar altimeter (RA2) to measure the nadir surface height along a predefined ground-track every 35 days. In October 2010, it accomplished an orbit lowering maneuver to extend mission life and entered a new "drifting phase" [54] of the mission: the orbit no longer followed exact ascending/descending nodes and a repeat cycle shortened to 30 days. Toward the end of April 2012, there was a sudden loss in communication that caused Envisat to be announced the end in cycle 113. The RA2 sensor data record (RA2_MWS_2P) and RA2 geophysical data record (RA2_GDR_2P) were archived for registered users via the ESA Earth Online data portal (Available: https://earth.esa.int/). Here, we used the latest version of reprocessed Envisat GDR (V2.1) provided by CNES Archiving, Validation, and Interpretation of Satellite Oceanographic data (AVISO) service in regular operation mode spanning 2002–2010, corresponding to cycle 6–93. We picked pass #406 near the Overton Arm of northern Lake Mead (Fig. 1), which had $\sim$3.5 km water crossover along track, or about ten 18 Hz footprints. The ICE-1 altimetry range retracker, performed by AVISO that had been proved adequate for inland water research [5], [18], was then used with several extra corrections, including geophysical (solid Earth tide and pole tide), atmospheric (dry/wet troposphere), ionospheric (path delay proportional to the total election content), and hardware (ultra stable oscillator) terms [55]. A random drift of ground track in $\pm$1 km was ignored. Finally, the height of water level, with respect to the WGS84 reference ellipsoid, at each 18 Hz Ku band measurement can be estimated at the overpass in Lake Mead.

For ICESat laser altimetry, the Global Land Surface Altimetry product number 14 (GLA14, release-33) was taken as the primary data to calculate water level changes. It is known that the ICESat only worked in campaign mode, mostly in February–March/May–June/October–November, 2003–2009, due to the failure in a pump diode array soon after launch. The ICESat data had been made available at the NASA's earth observing system clearing house (ECHO) online portal (Available: http://reverb.echo.nasa.gov). The data preprocessing, including saturation correction and cloud exclusion, was conducted by our algorithm identical to the method introduced in Wang *et al.* [8], [19]. After that, to calculate the precise water level changes, we chose the footprints with only one peak in the received waveform for further calculation because the footprint covering purely water surface normally forms a single peak pattern [19]. Lake margin was determined from Landsat ETM+ via a similar water index mask as introduced later in Section IV-B. For HD, we compared several images in wet season in 2003–2008, and chose Landsat 7 scene LE50390352003284LGS01 to extract water boundary, as its timing corresponding to the larger lake width that ensures more footprints coming into the final calculation. Since the river

width at this ICESat crossover is less than 1 km and the slope of shore is steep, the seasonality of river width is thus negligible in this case. A buffer region with $\sim$100 m as buffer radius was then generated to clip footprints covering the waters. In the end, the height based on its specific ellipsoid in a mean-tide system (similar to T/P and Jason-1) was then converted into WGS84 standard, and the averaged water levels and their standard deviations were calculated from along-track observations. Regarding to the quantity and quality of observations, the data obtained from ICESat campaigns were useful and stable over the water surface. The track covering lake surface was about 2.5 km, approximate 15 footprints on average.

4) In Situ Data: The WSH of Lake Mead at HD has been measured by the Bureau of Reclamation, U.S. Department of the Interior (Available: http://www.usbr.gov). The monthly average data published online were collected since 1935 based on an uncharted local datum. A long-term historical record with monthly WSH data allowed us to compare with TIAS estimates back to 1980s. Since the variation of water level is smooth in HD, without notable change excepting seasonal signal, we simply interpolated monthly record to the date when Landsat image was taken during the time span. Finally, the mismatch in vertical datum between gauge data and the TIAS was removed from the estimate of bias in the time series after entire TIAS operation.

B. Data Processing

1) MNDWI: The determination of shoreline in Landsat TM/ETM+ imagery can be accomplished by a couple of methods, e.g., the regular NDWI extraction or the single band (band 4, 750–900 nm) analysis. The MNDWI was first presented in Gao [56] to map the vegetation liquid water. McFeeters [57] later refined the model to extract water features by using green and near-infrared (NIR) bands, known as the modified NDWI (MNDWI). The form we adopted here is an improved MNDWI with bands selected by Xu [58], which used the shortwave-infrared (SWIR) instead of NIR in Ji *et al.* [59], to enhance the separation of built-up features in water area. Upon the computation of the MNDWI, we are able to differentiate water features from other landscape by using bands 2 and 5 in TM/ETM+. The MNDWI for Landsat is thus formulated as [58]

$$MNDWI_{Landsat} = \frac{Green - SWIR}{Green + SWIR} \tag{1}$$

where green is the Landsat TM/ETM+ band 2 at 520–600 nm and SWIR is the lower reflectance band 5 at 1550–1750 nm.

The principle behind this index is by revealing the difference between the strong and weak reflectance from water surface, with a normalization to avoid solar zenith angle alteration, to distinguish the high-contrast pattern in spectrum that matches the behavior of water molecules. The area of water surface is then discriminated from other surface types where the MNDWI of such pixel is higher than certain threshold. Since the threshold of MNDWI is an empirical number depending on the local mixture of landscape [59], we first selected 0.2 as threshold to compute and then tested between 0.15–0.25 to find the better setting. This iteration acting as a calibration purpose was used to find a threshold setting for certain DEM that results in lower RMSE compared with *in situ* data.

2) DEM Bathymetry Projection: To extend the terrain downward into water surface boundary existing in the original DEM, we linearly extrapolate the terrain surface from the nearby grids and assume that the slope remains constant. The pixelwise computation of bathymetry over water area is thus expressed as

$$H_i = H_j - S_j \times D_{ij} \tag{2}$$

where

- i pixel over lake to be extrapolated,
- j is the pixel closest to i with valid elevation in DEM,
- H_i is the height of bathymetry at pixel i,
- H_j is the height of land at pixel j,
- D_ij is the geometric distance between pixel i and j,
- S_j is the averaged slope computed from a 3×3 window centered at pixel j.

While there are multiple land points with the same closest distance to point i, we took an average of slope from these points and follow the same computation. As mentioned before, this method would probably underestimate the WSH when the lake level falls near the actual lake bottom since the lower bound of lake bottom had not been limited. However, this coarse approximation is sufficient to serve as a reference for few tens of meters movement in vertical, as the behavior of Lake Mead. As shown in Fig. 4, a comparison between original, modified, and real bathymetry is demonstrated. In this figure, the top and middle panels show the change of water surface mask and projected bathymetry exemplified by GMTED2010. The bottom panel is an actual survey provided by USGS (Available: http://pubs.usgs.gov/of/2003/of03-320/index.htm). It is observed that although some of the coastal areas have inaccurate bathymetry (e.g., near lon: 245.30 lat: 36.12 and lon: 245.36 lat: 36.14), and some islands that have been intentionally masked out, the slope of projected bathymetry matches mostly well with the USGS reference. Another example shown in Fig. 5 demonstrates the TIAS with ASTER GDEM2 before and after the bathymetry projection. The estimate of WSH using original DEM meets a lower bound at 350 m w.r.t. WGS84 ellipsoid while WSA shrinks to a smaller extent than the predefined water area (green square). Once we extend the terrain toward the lake center for hundreds of meters, the improved WSH estimates (blue cross) are allowed to access deeper contours based upon the modified DEM.

C. Water Level Extraction

1) WSH Histogram: After gathering all DEM values along the shoreline, we first eliminated outliers obviously out of bounds (e.g., $\text{deviation greater than} \pm 100\,\text{m}$) and then applied a standard 2σ data editing for initial filtering. The estimates would form a distribution with a spread of a few more than ten meters and centralizing within a few meters, as shown in Fig. 3 panel b. The histogram is then used to find the best estimate of WSH at certain scene by the following fitting function.

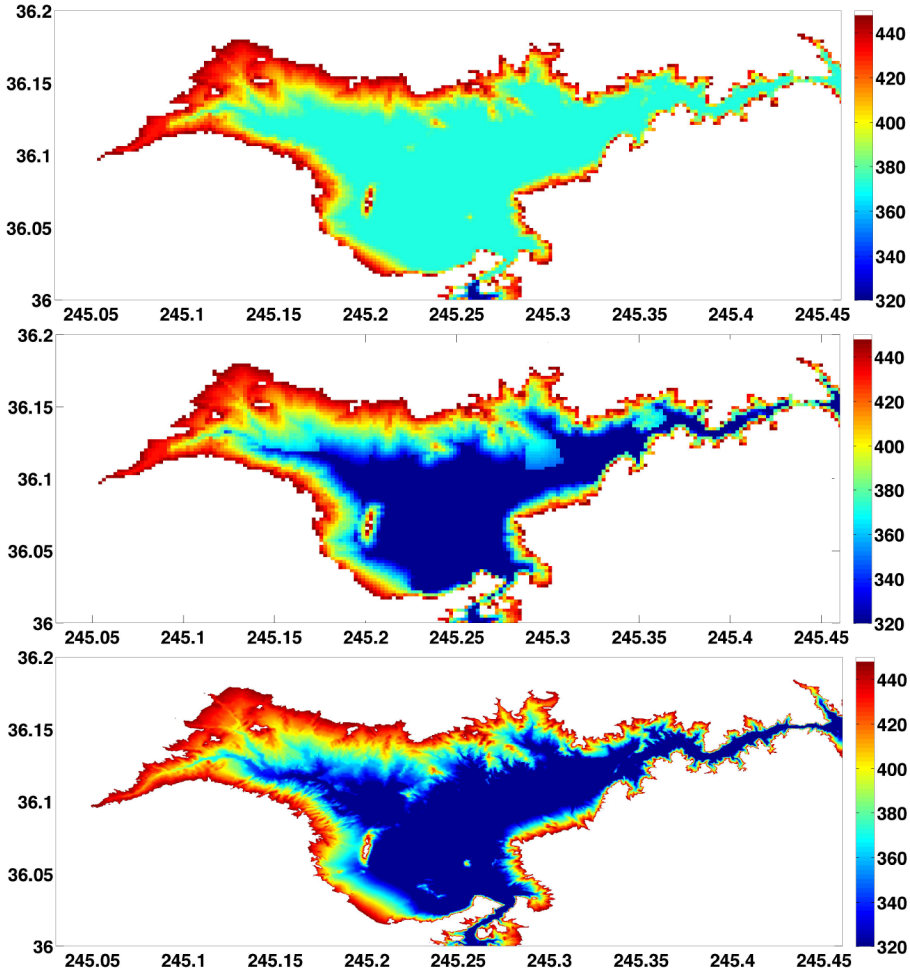

Fig. 4. Visual comparison of original (top), modified (middle), and real (bottom) bathymetry from the projection method. The original and modified DEM is GMTED2010 and the actual bathymetry is from USGS 1999 sidescan-sonar and chirp seismic-reflection survey. The color code covering the variation of water level during study time span is in meter.

2) Generalized Extreme Value (GEV) Fitting Function: Considering the DEM with internal vertical accuracy varying up to few tens of meters, in addition to the grid size of MNDWI that contains a horizontal ambiguity of at least 30 m, the histogram of WSH samples thus has extreme values centered at a few meters where the tail of the pdf is relatively prolonged. Therefore, we chose the GEV distribution to model the peak value among a collection of samples. The density function of the GEV distribution is expressed as [47], [60]–[61]

$$y = f(x|\mu,\sigma,\xi) = \left(\frac{1}{\sigma}\right) \times \exp\left(-\left(1+\xi\frac{(x-\mu)}{\sigma}\right)^{-\frac{1}{\xi}}\right)\left(1+\xi\frac{(x-\mu)}{\sigma}\right)^{-1-\frac{1}{\xi}} \tag{3}$$

for

$$1+\xi\frac{(x-\mu)}{\sigma} > 0 \tag{4}$$

where μ, σ, and ζ are the location, scale, and shape parameters, respectively.

We exploit the GEV fitting function namely *gevfit* compiled by the MATLAB Statistics Toolbox to resolve the fitting parameters. The *gevfit* function fits the histogram by the maximum log-likelihood estimation. It first obtains initial parameters from the P–P (probability–probability) plot of input data (i.e., WSH) over the shape parameter, and then iterates to maximize the log-likelihood with respect to the parameters until convergence. The fitting procedure is applied to each of the 584 scenes and a typical example of fitting result is also shown as green line in Fig. 3 panel *b*.

V. Results and Discussion

A. TIAS Versus In Situ

The temporal comparison of WSH anomaly estimated by the TIAS with MNDWI threshold equal 0.2, radar altimetry, and gauge data in HD is shown in Fig. 6. Fig. 6(a) displays that the TIAS estimates using a paired Landsat images and ASTER GDEM2 (blue dot) yield a fairly good agreement with *in situ* data (red line) during the comparing time span. Although the Envisat ICE-1 retracked results (green circle) provide better quality measurements at this location, we could see the

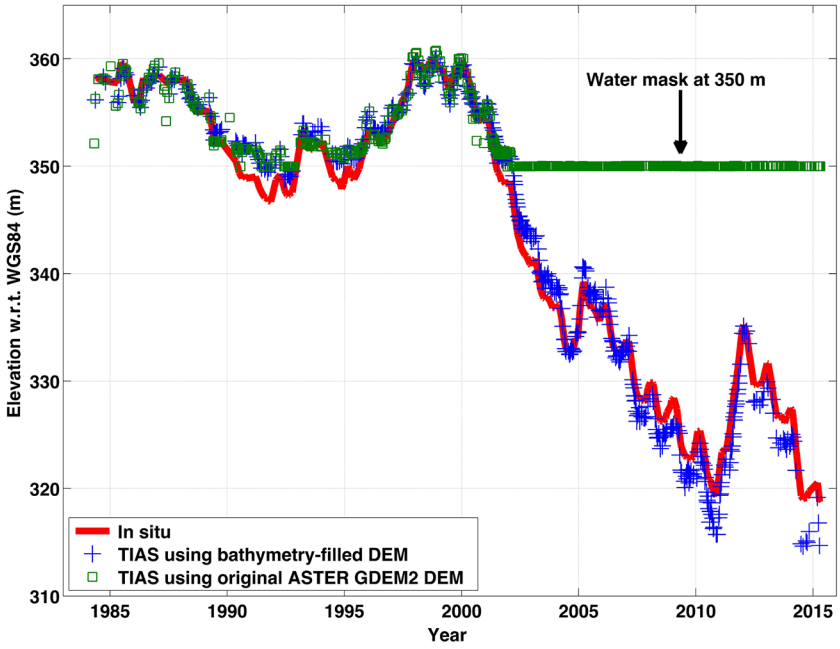

Fig. 5. Temporal comparison of TIAS WSH estimates using raw ASTER GDEM2 (green square) and modified DEM (blue cross), and compared with *in situ* gauge data (red line). The TIAS is unable to yield correct results below ∼350 m while using the original DEM. Instead, the modified DEM with simulated bathymetry successfully allow TIAS to recover the WSH below a predefined water mask. Two TIAS time series shown here have been applied a regular 2σ data editing against the three-point moving average itself for visual clarification. A datum offset at 6.44 m is removed for *in situ* data.

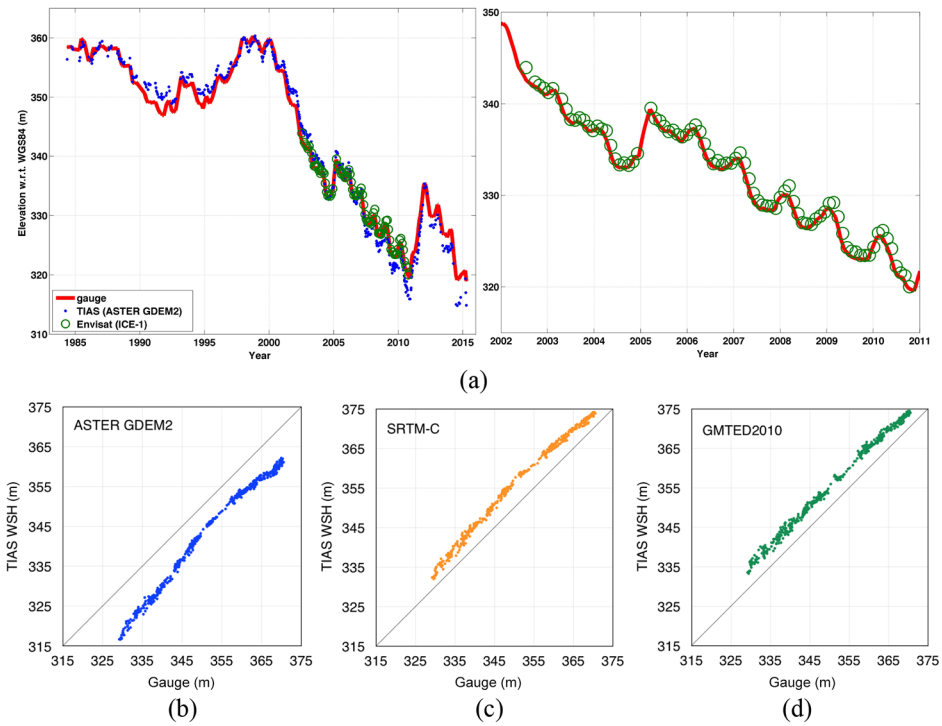

Fig. 6. Panel (a, left): the TIAS time series using ASTER GDEM2 (blue dot) and compared with gauge data (red line) and Envisat altimetry (green circle). Panel (a, right): a zoom-in of left panel in 2002–2011 during Envisat time span. Panel (b), (c), and (d) is to compare gauge record (x-axis) with TIAS WSH (y-axis) using ASTER GDEM2, SRTM-C, and GMTED2010, respectively.

temporal restriction for Envisat, in terms of a shorter mission span and a coarser 35-day repeat period.

The lower panel of Fig. 6 performs the intercomparison between three DEMs while using identical RS images as input, and is validated with gauge data. It is observed that all of these three DEMs are capable to yield excellent agreement with gauge data, with R^2 values equal to 0.99 for all, while GMTED2010 seems the best among them without any specific deficiency in any altitude. In contrast, the ASTER GDEM2 has a slight unmatched height near 350 m w.r.t. WGS84, which

TABLE II
STATISTICAL RESULTS OF THE TIAS AND ALTIMETRY SATELLITES MEASURED WSH COMPARED WITH INTERPOLATED *IN SITU* DATA IN VARIOUS TIME SPANS

			Before de-outlier	After de-outlier			
	DEM	MNDWI threshold	RMSE (m) (± 95% CI)	RMSE (m) (± 95% CI)	R^2	Pres. rate (%)	N
TIAS (Landsat TM/ETM+, 1983–2015)	SRTM C-band	0.15	1.15 ± 0.54	1.12 ± 0.53	0.99	93	543
		0.20	1.09 ± 0.55	1.03 ± 0.53	0.99	90	528
		0.25	1.19 ± 0.55	0.98 ± 0.54	0.99	89	522
	ASTER GDEM2	0.15	1.67 ± 0.45	1.62 ± 0.43	0.99	92	536
		0.20	1.83 ± 0.46	1.74 ± 0.44	0.99	90	523
		0.25	2.06 ± 0.47	1.90 ± 0.45	0.99	87	507
	GMTED 2010	0.15	1.01 ± 0.63	0.97 ± 0.63	0.99	94	550
		0.20	0.97 ± 0.64	0.86 ± 0.63	0.99	92	539
		0.25	1.15 ± 0.64	0.85 ± 0.63	0.99	91	530
ICESat (2003–2009)			–	0.39 ± 0.08	0.99	87	20
Envisat (2002–2010)			–	0.38 ± 0.10	0.99	95	82

The first column name **"**Before de-outlier**"** numerates the $\mathrm{RMSE} \pm 95\%$ confidence interval of the TIAS estimates (entire Landsat dataset) compared with *in situ* data. The second column name **"**After de-outlier**"** numerates the $\mathrm{RMSE} \pm 95\%$ confidence interval of the TIAS estimates after 2σ de-outlier from the moving average itself and compared with *in situ* data. R^2 is square of the Pearson correlation coefficient. The preservation rate (Pres. Rate) indicates the percentage of height measurements preserved after calibration, where N is the correspondent number of preserved Landsat images. By using different MNDWI threshold, N will change accordingly due to the inclusion or discard of TIAS points from certain Landsat scenes.

corresponds to the same interval in the top panel. The disagreement, due to the inaccuracy of raw or modified DEM at that elevation and the slope change, degrade the correlation with gauge data. A systematic offset between gauge measurement and TIAS WSH is also noticed in this panel. It is basically due to the difference in absolute height.

In Table II, we examined the effectiveness among DEMs in TIAS and compared the results with altimetry data. Moreover, we tested different MNDWI threshold to reveal its role in the TIAS computation. The left part (before de-outlier) of Table II is the comparison between entire RS imagery dataset and gauge data, without any data selection, where the right part (after de-outlier) is the comparison using de-outlier time series based on the moving average itself. As shown in the TIAS part of Table II, a de-outlier process that removes anomalous estimates generally improves the accuracy at 3–30 cm, which effectively discards 6–13% of data during self-check. The best result is 0.85 ± 0.63 m while using GMTED2010 with MNDWI threshold set to 0.25, and the worst one is 1.90 ± 0.45 m while using ASTER GDEM2 with MNDWI threshold set to 0.25, after de-outlier. Although GMTED2010 has the coarser resolution in this comparison, it gives the best results compared with others. The reason is because it took SRTM as its core data, especially in the study area (as shown in Table I); hence, the TIAS result varies similarly with SRTM C-band solutions. The extra improvement it has made is because of its smoothness, which seems to be a shortcoming intuitively, actually yields a less variable bathymetry, compared with SRTM C-band. For 30 m SRTM C-band and ASTER GDEM2, the extrapolated bathymetry is more fluctuating and some of the grids are treated as noise in the fitting procedure. For ASTER GDEM2, the actual vertical accuracy may be a bit worse than SRTM, especially over mountain region [46].

In addition, the optimal threshold setting differs case by case and depends mainly on the DEM in use. Overall, the reference value at 0.2 remains the best or second in the midst of three options, and a change in threshold just marginally alters the result. This is because the DEM accuracy over mountain area and the effect of slope change has larger uncertainty that overrides the difference between these three thresholds. The fine-adjustment between 0.15 and 0.25 may not be significant for the determination of TIAS WSH estimates unless we have a higher resolution DEM. Nevertheless, the selection of threshold can be considered once there is *in situ* data available and this calibration step is executable at study site.

In the lower part of Table II, radar/laser altimetry measurements are also listed for a qualitative comparison, although the sampling time was different from Landsat imagery. The statistical results maintaining high accuracy at 0.38–0.39 m in RMSE are similar to the results reported in other studies [62], despite the narrow water surface width that only allows few points of measurements in Lake Mead. In contrast, based on the limited resolution of tested DEMs and Landsat imagery used in this study, which are 30 m at highest for both, the best result of the TIAS is 0.85 ± 0.63 m. This fact implies that the current form of TIAS can only be used to monitor water level change larger than meter level. It needs further improvement to achieve higher accuracy, e.g., using higher resolution RS imagery and local DEM.

Another point worthwhile to mention is the temporal sampling rate of each radar, laser, or the TIAS approach. The common revisit period for current radar altimetry satellites, e.g., Jason-2 and SARAL/AltiKa, is 10 and 35-day, respectively, if they had a fly-by at these locations. For the not fully operated ICESat-1, the repeat cycle, by design, would be 91-day. The TIAS has repeat observation at least every 16-day along with the revisit of multiple Landsat satellites. However, the temporal sampling of the TIAS is not regular and heavily depends on the regional climate, such as pertaining cloud cover in rainy season. Therefore, at HD there is a sampling rate of $\sim$20-day if we take 584 usable scenes as a benchmark in its 32-years period. The temporal resolution can be potentially improved in later years and in the near future since there are many other optical sensors operating in space.

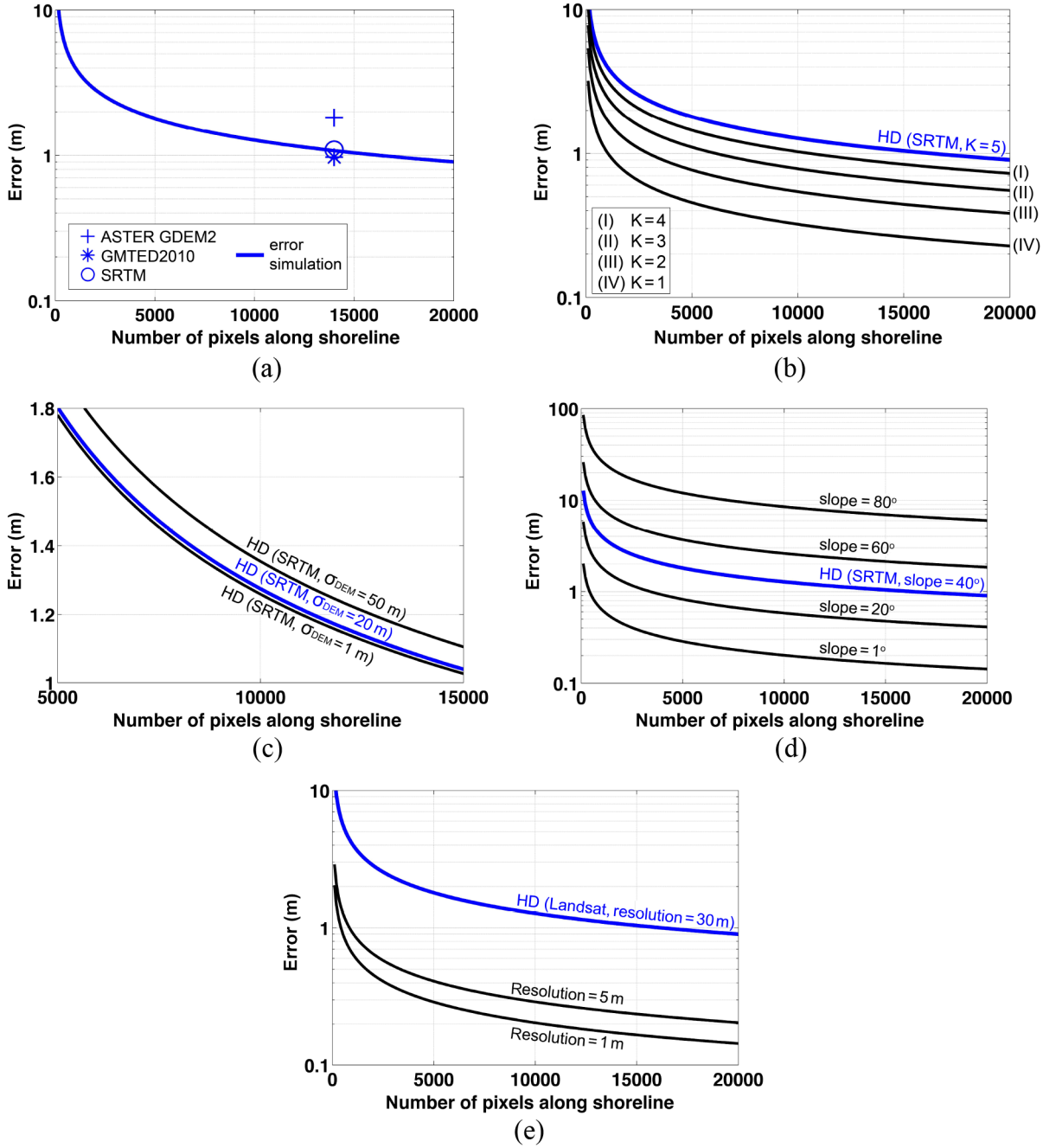

Fig. 7. Error analysis and sensitivity test for several error components, namely, shoreline positioning uncertainty (K), vertical random error in DEM (σ_{DEM}), terrain slope (ϑ), and RS imagery/DEM resolution (R_{rs}). The blue line used for all panels as a reference is specified as: K $= 5$, $\sigma_{\mathrm{DEM}} = 20$ m, $\vartheta = 40°$, and $R_{rs} = 30$ m. (a) A simulation of error budget (in meter) as a function of the number of pixel along shoreline, i.e., dividing the shoreline length by pixel size. Error of the TIAS estimates associated with three DEMs is given by different symbols at corresponding abscissa locations. (b) Error associated with horizontal uncertainty. The error reduced from meter level to $<$50 cm when the value of K in (6) reduces to 1 or 2. (c) Error change as a function of varying DEM relative vertical accuracy. In this case, the change among 1–50 m slightly altered the error budget in just few centimeters due to an abundance of n. (d) The change of error budget together with terrain slope change, which is the most dominant factor in this analysis. The value of ϑ varying from 80°–1° altered the error from about 10 m to 0.2 m level when n is about 15 000. (e) A simulation of error while using other RS imagery and DEM sources with smaller pixel size. The error could be reduced to 0.2 m level with pixel size in 1 m.

B. Error Budget and Sensitivity Analysis

To understand error sources and to explore potential improvement of the TIAS, we analyze the error propagation and test the sensitivity of several components. The errors propagating to the computation of final RMSE (compared with *in situ* data) are complicated, at least involving the horizontal/vertical accuracy of DEM, resolution, and quality of RS imagery, relative error due to coregistration, terrain slope, number of observations, and uncertainty of the MNDWI classification. Here, we simplify the problem and analyze a couple of dominating factors to check the sensitivity of each component contributing to the final result. A major part of total error as compared with

in situ data at each snapshot, as denoted by σ_{T} in the following equation (5), is associated with the random error in DEM σ_{DEM}, the terrain slope σ_{Slope} that renders the ratio of water level change along with extent change, and the number of shoreline pixels n within one Landsat image that efficiently reduce random errors in DEM.

$$\sigma_T = \sqrt{\frac{\sigma^2{}_{DEM} + \sigma^2{}_{Slope}}{n}}. \tag{5}$$

In (5), the vertical uncertainty associated with terrain slope has a range defined as

$$\sigma_{Slope} = K \times R_{rs} \tan\theta \tag{6}$$

where R_{rs} is the pixel size (i.e., 30 m for Landsat) in meter, ϑ is the terrain slope in degree, and K is the general scaling factor indicating horizontal accuracy of DEM and MNDWI classification error.

By simulating the total error from above-mentioned variables, we gave a set of sample inputs to generate a figure as shown in Fig. 7, where the ordinate of panel a, b, d, and e is in log scale. In Fig. 7(a), σ_{DEM} equal 20 m and K equal 5 were selected as a starting point to match the predicted errors with our results. The number of pixel is set to 14 000 for TIAS results and a variation of ± 1500 may occur in this case. Here, the reference of vertical error at 20 m is reasonable since the accuracy of DEMs used here is usually less reliable in mountain area, where the RMSE is higher than the original specification, i.e., 10–20 m [63]. In Fig. 7(a), the slope of terrain [ϑ in (6)] is set 40° for HD, corresponding to the average slope plus 2σ computed from SRTM-C within the water variation interval (i.e., 320–375 m in HD). In this panel, we observe that the error drops significantly as the number of pixels along the shoreline increases. The TIAS error is about the same level as analysis from (5) at HD (blue symbols), except for the slightly higher error computed by ASTER GDEM2 (+symbol).

In Fig. 7(b)–(e), we took the setting of Fig. 7(a) as the reference to test the sensitivity of error component one at a time. In Fig. 7(b), the error decreases along with the descending value of K, from 5 to 1, meaning the combined error of shoreline delineation and DEM horizontal accuracy decrease from 5 to 1 pixel can effectively reduces the error to submeter level. It implies that our current method may consist of a notable uncertainty in water outline determination. A more sophisticated decision tree may be needed to reduce the horizontal error and to achieve a better shoreline positioning. However, it is emphasized that the final RMSE is a combined error with other components, such as the slope shown later in Fig. 7(d), hence the initial value of K picked here may be exaggerated. Next, in Fig. 7(c), while switching the relative vertical error in DEM, from 20 m to 1 m and 50 m, the corresponding error varies only within about 10 cm at the study site. Hence, the random error in DEM is less critical in the computation of water level while dealing with a water body at similar size. In Fig. 7(d), we tested the error budget associated with the change of terrain slope, including 1°, 20°, 40° (HD case), 60°, and 80°, to examine the potential error changes accordingly. In this panel, we observe the error increases significantly as the slope elevates, from 0.2 m (at 1° slope) to 6 m (at 80° slope), if we kept other settings in HD case fixed as reference. It is known that in HD, a part of lakeside terrain has a slope greater than 40°, which contribute to a great portion of error in the final RMSE. For other lakes in the world, the application of TIAS should consider avoiding steep part of terrain and use only flatter area while the pixel number (shoreline length) allows.

Finally, the errors associated with the pixel size of both RS imagery and DEM are shown in Fig. 7(e). In Fig. 7(e), the prospective application of the TIAS is revealed as we see the error budget decreases significantly when the pixel size shrinks to 5 or 1 m level. It is noted that the equivalent lake size has become smaller accordingly in this figure, while the number of pixels along the shoreline remains and the size of each pixel downscales. For example, in the simulation of 1 m resolution the x-axis at 10 000 corresponding to a total length of shoreline equal 10 km, and the errors remaining perhaps reach 20 cm level. Therefore, use of ultrahigh-resolution optical or radar images will boost the applicability of this method prominently.

VI. Conclusion

In this study, we demonstrated a possibility to recover the inland WSH via the TIAS, an indirect measure that incorporates a horizontal swath of satellite imaging sensors/instruments and a referenced DEM. In order to obtain a promising result, several assumptions are needed to uphold the proposed technique: 1) the shore should be less steep for detection of WSA changes as WSH varies; 2) the WSH variation must exceed current limitation in accuracy, say >1 m; and 3) the bathymetry, if not available in a DEM, will be assumed a constant slope. Here are also some uncertainties need to be considered: 1) the accuracy depends on the DEM and RS imagery in use; 2) extra uncertainty introduced by aligning RS imagery and DEM and the following double-linear interpolation has not been considered; and 3) regional variability of bathymetry slope may lead to a decreased accuracy once the water level drop into the simulated DEM section, and the uncertainty increases as the WSH approaches lake bottom. Nevertheless, the TIAS at presented study site, HD in Lake Mead, yields an accuracy of WSH estimate up to 0.85 m and an excellent correlation with groundtruth data. It satisfies the needs in a broad range of hydrological and limnological studies elsewhere in the world, especially for lakes that are experiencing extreme variations in height and are isolated without sufficient *in situ* data, or whose location is out of the flight path of current radar/laser altimetry satellites. Although a lot of concerns may have placed to the data availably in this study: the Landsat 4 was decommissioned in 2001, Landsat 5 stopped working in November 2011, and Landsat 7 suffers a long-term degradation in gains. The TIAS will incorporate the newly launched Landsat 8 as well as other optical instruments in the community, to conduct a prospective/retrospective analysis and operational observation. More importantly, the higher resolution (<30 cm) is achievable by using high or ultra high-resolution commercial RS imagery, based on the error analysis. In the future, we will also

use other altimetry satellite data, such as reprocessed Jason-1/-2, TOPEX/Poseidon and SARAL/AltiKa, to elongate the altimetry time series for validation of this technique in other major lakes

REFERENCES

[1] D. E. Alsdorf, E. Rodriguez, and D. P. Lettenmaier, "Measuring surface water from space," *Rev. Geophys.*, vol. 45, no. 2, pp. 1–24, May 2007.

[2] M. Durand, L. L. Fu, D. P. Lettenmaier, D. E. Alsdorf, E. Rodriguez, and D. Esteban-Fernandez, "The surface water and ocean topography mission: Observing terrestrial surface water and oceanic submesoscale eddies," *Proc. IEEE*, vol. 98, no. 5, pp. 766–779, May 2010.

[3] S. Biancamaria, F. Hossain, and D. P. Lettenmaier, "Forecasting transboundary river water elevations from space," *Geophys. Res. Lett.*, vol. 38, L11401, pp. 1–5, 2011.

[4] P. A. M. Berry, H. Bracke, and A. Jasper, *Retracking ERS-1 Altimeter Waveforms Over Land for Topographic Height Determination: An Expert Systems Approach*. Eur. Space Agency Spec. Publ., ESA SP-414, 1997, pp. 403–408.

[5] F. Frappart, S. Calmant, M. Cauhope, F. Seyler, and A. Cazenave, "Preliminary results of ENVISAT RA-2-derived water levels validation over the Amazon basin," *Remote Sens. Environ.*, vol. 100, no. 2, pp. 252–264, 2006.

[6] S. Calmant, F. Seyler, and J. F. Cretaux, "Monitoring continental surface waters by satellite altimetry," *Surveys Geophys.*, vol. 29, nos. 4–5, pp. 247–269, Oct. 2008.

[7] C. M. Birkett and B. Beckley, "Investigating the performance of the Jason-2/OSTM radar altimeter over lakes and reservoirs," *Mar. Geod.*, vol. 33, pp. 204–238, 2010.

[8] X. W. Wang *et al.*, "Water-level changes in China's large lake determined from ICESat/ GLAS data," *Remote Sens. Environ.*, vol. 132, no. C, pp. 131–144, 2013.

[9] *OSTM/Jason-2 Products Handbook*, JPL Standard OSTM-29-1237, 2009.

[10] J. Lambin *et al.*, "The OSTM/Jason-2 mission," *Mar. Geod.*, vol. 33, pp. 4–25, Oct. 2010.

[11] W. Abdalati *et al.*, "The ICESat-2 laser altimetry mission," *Proc. IEEE*, vol. 98, no. 5, pp. 735–751, May 2010.

[12] R. D. Koster, P. R. Houser, E. T. Engman, and W. P. Kustas, "Remote sensing may provide unprecedented hydrological data," *Eos Trans. Amer. Geophys. Union*, vol. 80, no. 14, p. 156, Apr. 1999.

[13] C. K. Shum *et al.*, "Calibration of JASON-1 altimeter over lake erie special issue: Jason-1 calibration/validation," *Mar. Geod.*, vol. 26, nos. 3–4, pp. 335–354, 2003.

[14] P. A. M. Berry, J. D. Garlick, J. A. Freeman, and E. L. Mathers, "Global inland water monitoring from multi-mission altimetry," *Geophys. Res. Lett.*, vol. 32, no. 16, p. L16401, Aug. 2005.

[15] C. Hwang, Y.-C. Kao, and N. Tangdamrongsub, "A preliminary analysis of lake level and water storage changes over lakes Baikal and Balkhash from satellite altimetry and gravimetry," *Terr. Atmos. Ocean. Sci.*, vol. 22, pp. 97–108, 2011.

[16] J.-W. Kim *et al.*, "Integrated analysis of PALSAR/Radarsat-1 InSAR and ENVISAT altimeter data for mapping of absolute water level changes in Louisiana wetlands," *Remote Sens. Environ.*, vol. 113, pp. 2356–2365, 2009.

[17] M. Zhang *et al.*, "Application of retracked satellite altimetry for inland hydrologic studies," *Int. J. Remote Sens.*, vol. 31, pp. 3913–3929, 2010.

[18] H. Lee, C. Shum, K.-H. Tseng, J.-Y. Guo, and C.-Y. Kuo, "Present-day lake level variation from Envisat altimetry over the Northeastern Qinghai-Tibetan plateau: Links with precipitation and temperature," *Terr. Atmos. Ocean. Sci.*, vol. 22, pp. 169–175, 2011.

[19] X. Wang *et al.*, "Lake water footprint identification from time-series ICESat/GLAS data," *IEEE Geosci. Remote Sens. Lett.*, vol. 9, no. 3, pp. 333–337, May 2012.

[20] K. Tseng *et al.*, "Envisat altimetry radar waveform retracking of quasi-specular echoes over ice-covered Qinghai lake," *Terr. Atmos. Ocean. Sci.*, vol. 24, no. 4, pp. 615–627, 2013.

[21] C. Birkett, "The contribution of TOPEX/POSEIDON to the global monitoring of climatically sensitive lakes," *J. Geophys. Res. Oceans*, vol. 100, pp. 25179–25204, 1995.

[22] S. Calmant and F. Seyler, "Continental surface waters from satellite altimetry," *Comptes Rendus Geosci.*, vol. 338, pp. 1113–1122, 2006.

[23] H. Lee, C. Shum, K.-H. Tseng, Z. Huang, and H.-G. Sohn, "Elevation changes of bering glacier system, Alaska, from 1992 to 2010, observed by satellite radar altimetry," *Remote Sens. Environ.*, vol. 132, pp. 40–48, 2013.

[24] X. Deng, W. Featherstone, C. Hwang, and P. Berry, "Estimation of contamination of ERS-2 and POSEIDON satellite radar altimetry close to the coasts of Australia," *Mar. Geod.*, vol. 25, no. 4, pp. 249–271, 2002.

[25] L. Yang, M. Lin, Q. Liu, and D. Pan, "Retracking strategy based on waveform classification and sub-waveform extraction for coastal altimetry along China coastal seas," in *Proc. IEEE Int. Geosci. Remote Sens. Symp. (IGARSS)*, 2010, pp. 632–635.

[26] K.-H. Tseng *et al.*, "The improved retrieval of coastal sea surface heights by retracking modified radar altimetry waveforms," *IEEE Trans. Geosci. Remote Sens.*, vol. 52, no. 2, pp. 991–1001, Feb. 2014.

[27] C.-Y. Kuo and H.-C. Kao, "Retracked Jason-2 altimetry over small water bodies: Case study of Bajhang River, Taiwan," *Mar. Geod.*, vol. 34, no. 3–4, pp. 382–392, 2011.

[28] H. Lee, M. Durand, H. C. Jung, D. Alsdorf, C. Shum, and Y. Sheng, "Characterization of surface water storage changes in Arctic lakes using simulated SWOT measurements," *Int. J. Remote Sens.*, vol. 31, no. 14, pp. 3931–3953, 2010.

[29] F. Frappart *et al.*, "Surface freshwater storage and dynamics in the Amazon basin during the 2005 exceptional drought," *Environ. Res. Lett.*, vol. 7, no. 4, p. 044010, 2012.

[30] R. K. Raney, "The delay/Doppler radar altimeter," *IEEE Trans. Geosci. Remote Sens.*, vol. 36, no. 5, pp. 1578–1588, Sep. 1998.

[31] F. Frappart, F. Seyler, J.-M. Martinez, J. G. Leon, and A. Cazenave, "Floodplain water storage in the Negro River basin estimated from microwave remote sensing of inundation area and water levels," *Remote Sens. Environ.*, vol. 99, pp. 387–399, 2005.

[32] F. Frappart *et al.*, "Water volume change in the lower Mekong from satellite altimetry and imagery data," *Geophys. J. Int.*, vol. 167, pp. 570–584, 2006.

[33] Z. Duan and W. Bastiaanssen, "Estimating water volume variations in lakes and reservoirs from four operational satellite altimetry databases and satellite imagery data," *Remote Sens. Environ.*, vol. 134, pp. 403–416, 2013.

[34] L. C. Smith and T. M. Pavelsky, "Remote sensing of volumetric storage changes in lakes," *Earth Surf. Processes Landforms*, vol. 34, p. 1353, 2009.

[35] B. Marti-Cardona, C. Lopez-Martinez, J. Dolz-Ripolles, and E. Bladè-Castellet, "ASAR polarimetric, multi-incidence angle and multitemporal characterization of Doñana wetlands for flood extent monitoring," *Remote Sens. Environ.*, vol. 114, pp. 2802–2815, 2010.

[36] R. Abarca-Del-Rio, J.-F. CrÉtaux, M. Berge-Nguyen, and P. Maisongrande, "Does Lake Titicaca still control the Lake Poopó system water levels? An investigation using satellite altimetry and MODIS data (2000–2009)," *Remote Sens. Lett.*, vol. 3, pp. 707–714, 2012.

[37] K. W. Forsythe, B. Schatz, S. J. Swales, L.-J. Ferrato, and D. M. Atkinson, "Visualization of lake mead surface area changes from 1972 to 2009," *ISPRS Int. J. GeoInf.*, vol. 1, pp. 108–119, 2012.

[38] H. Gao, C. Birkett, and D. P. Lettenmaier, "Global monitoring of large reservoir storage from satellite remote sensing," *Water Resour. Res.*, vol. 48, W09504, pp. 1–12, 2012.

[39] A. Pietroniro, T. Prowse, and D. Peters, "Hydrologic assessment of an inland freshwater delta using multi-temporal satellite remote sensing," *Hydrol. Processes*, vol. 13, pp. 2483–2498, 1999.

[40] K. Xu, J. Zhang, M. Watanabe, and C. Sun, "Estimating river discharge from very high-resolution satellite data: A case study in the Yangtze River, China," *Hydrol. Processes*, vol. 18, pp. 1927–1939, 2004.

[41] R. Andreoli, J. Li, and H. Yesou, "Flood extent prediction from lake heights and water level estimation from flood extents using river gauges, elevation models and ENVISAT data," in *Proc. ENVISAT Symp.*, Montreux, Switzerland, Apr. 23–27, 2007, (ESA SP-636, Jul. 2007).

[42] X. Cai, W. Gan, W. Ji, X. Zhao, X. Wang, and X. Chen, "Optimizing remote sensing-based level—Area modeling of large lake wetlands: Case study of Poyang Lake," *IEEE J. Sel. Topics Appl. Earth Observ. Remote Sens.*, vol. 8, no. 2, pp. 471–479, Feb. 2015.

[43] R. Q. Grafton *et al.*, "Global insights into water resources, climate change and governance," *Nat. Clim. Change*, vol. 3, pp. 315–321, 2013.

[44] A. Serrat-Capdevila, J. B. Valdes, F. Dominguez, and S. Rajagopal, "Characterizing the water extremes of the new century in the US Southwest: A comprehensive assessment from state-of-the-art climate model projections," *Int. J. Water Resour. Dev.*, vol. 29, pp. 152–171, 2013.

[45] S. L. Castle, B. F. Thomas, J. T. Reager, M. Rodell, S. C. Swenson, and J. S. Famiglietti, "Groundwater depletion during drought threatens future water security of the Colorado River Basin," *Geophys. Res. Lett.*, vol. 41, pp. 5904–5911, 2014.
[46] E. Suwandana, K. Kawamura, Y. Sakuno, E. Kustiyanto, and B. Raharjo, "Evaluation of ASTER GDEM2 in comparison with GDEM1, SRTM DEM and topographic-map-derived DEM using inundation area analysis and RTK-dGPS data," *Remote Sens.*, vol. 4, pp. 2419–2431, 2012.
[47] S. Kotz and S. Nadarajah, *Extreme Value Distributions*. Singapore: World Scientific, 2000, vol. 31.
[48] J. E. Morrison and J. A. Smith, "Stochastic modeling of flood peaks using the generalized extreme value distribution," *Water Resour. Res.*, vol. 38, pp. 41-1–41-12, 2002.
[49] G. Chander, B. L. Markham, and D. L. Helder, "Summary of current radiometric calibration coefficients for Landsat MSS, TM, ETM+, and EO-1 ALI sensors," *Remote Sens. Environ.*, vol. 113, pp. 893–903, 2009.
[50] T. Tachikawa *et al.* (2011). *ASTER Global Digital Elevation Model Version 2—Summary of Validation Results*, ASTER GDEM Validation Team [Online]. Available: http://www.jspacesystems.or.jp/ersdac/GDEM/ver2Validation/Summary_GDEM2_validation_report_final.pdf
[51] J. Danielson and D. Gesch, "Global multi-resolution terrain elevation data 2010," US Department of the Interior and US Geological Survey, 2011.
[52] C. C. Carabajal, D. J. Harding, J.-P. Boy, J. J. Danielson, D. B. Gesch, and V. P. Suchdeo, "Evaluation of the global multi-resolution terrain elevation data 2010(GMTED2010) using ICESat geodetic control," in *Proc. Int. Symp. Lidar Radar Mapping Technol.*, 2011, pp. 82861Y–82861Y-13.
[53] T. G. Farr and M. Kobrick, "Shuttle radar topography mission produces a wealth of data," *Eos Trans. Amer. Geophys. Union*, vol. 81, pp. 583–585, 2000.
[54] P. Schaeffer, Y. Faugere, J. Legeais, A. Ollivier, T. Guinle, and N. Picot, "The CNES_CLS11 global mean sea surface computed from 16 years of satellite altimeter data," *Mar. Geod.*, vol. 35, pp. 3–19, 2012.
[55] K. H. Tseng *et al.*, "Regional validation of Jason-2 dual-frequency ionosphere delays," *Mar. Geod.*, vol. 33, pp. 272–284, 2010.
[56] B. C. Gao, "NDWI—A normalized difference water index for remote sensing of vegetation liquid water from space," *Remote Sens. Environ.*, vol. 58, pp. 257–266, 1996.
[57] S. McFeeters, "The use of the normalized difference water index (NDWI) in the delineation of open water features," *Int. J. Remote Sens.*, vol. 17, pp. 1425–1432, 1996.
[58] H. Xu, "Modification of normalised difference water index (NDWI) to enhance open water features in remotely sensed imagery," *Int. J. Remote Sens.*, vol. 27, pp. 3025–3033, 2006.
[59] L. Ji, L. Zhang, and B. Wylie, "Analysis of dynamic thresholds for the normalized difference water index," *Photogramm. Eng. Remote Sens.*, vol. 75, pp. 1307–1317, 2009.
[60] A. F. Jenkinson, "The frequency distribution of the annual maximum (or minimum) values of meteorological elements," *Quart. J. Roy. Meteorol. Soc.*, vol. 81, pp. 158–171, 1955.
[61] P. Embrechts, C. Klüppelberg, and T. Mikosch, *Modelling Extremal Events*. New York, NY, USA: Springer, 1997, vol. 33.
[62] A. C. Hall, G. J. P. Schumann, J. L. Bamber, P. D. Bates, and M. A. Trigg, "Geodetic corrections to Amazon river water level gauges using ICESat altimetry," *Water Resour. Res.*, vol. 48, W06602, pp. 1–6, 2012.
[63] J. Thomas, S. Joseph, K. Thrivikramji, and K. Arunkumar, "Sensitivity of digital elevation models: The scenario from two tropical mountain river basins of the Western Ghats, India," *Geosci. Front.*, vol. 5, pp. 893–909, 2014.

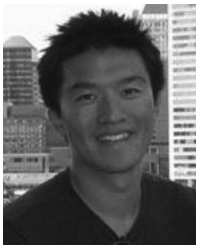

Kuo-Hsin Tseng received the B.S. degree in civil engineering from National Chiao-Tung University, Taiwan, in 2005 and the Ph.D. degree in geodetic science from the Ohio State University, OH, USA, in 2012.

He is currently an Assistant Professor in the Center for Space and Remote Sensing Research, National Central University, Taiwan. He is also with the Institute of Hydrological and Oceanic Sciences (IHOS) and with the Department of Civil Engineering, NCU. His researches are focused on satellite radar/laser altimetry, GNSS, and various applications by using satellite remote sensing.

C.K. Shum received the Ph.D. degree in aerospace engineering from University of Texas at Austin, Austin, TX USA, in 1982.

He is currently a Professor and Distinguished University Scholar, Division of Geodetic Science, School of Earth Sciences, Ohio State University, OH, USA. His research interests include the accurate measurements and the improved understanding of the geophysical causes of the 20th century and present-day sea-level rise, and cross-disciplinary Earth sciences, using a variety of space geodetic and in situ measurements, including satellite altimetry, gravimetry, GNSS, and synthetic aperture radar interferometry.

He is a Fellow of the International Association of Geodesy, and the American Association for the Advancement of Science.

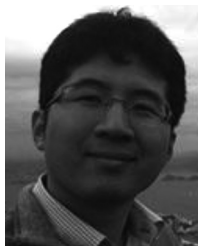

Jin-Woo Kim received the Ph.D. degree from the Division of Geodetic Science of the Ohio State University, OH, USA, in 2013.

He has been with Roy M. Huffington Department of Earth Sciences at the Southern Methodist University, TX USA, since 2014, where he works as the research scientist for the radar laboratory. His research interests include the applications of spaceborne synthetic aperture radar data processing and interferometry toward wetland and geohazard monitoring.

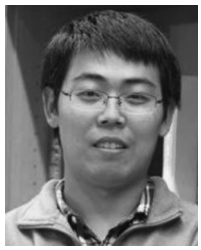

Xianwei Wang received the B.S. degree in engineering of surveying and mapping from College of GeoExploration Science and Technology, Jilin University, Jilin, China, in 2007 and the Ph.D. degree from the Institute of Remote Sensing Applications, Chinese Academy of Sciences, Beijing, China, in 2012.

In October 2013, he was working as a postdoctoral associate at the New York University Abu Dhabi, UAE. Currently, he is a research scientist in Center for Global Sea Level Change in New York University Abu Dhabi, UAE. His research interests include the snow and ice changes in cryosphere and lake level changes under the background of global change by using remote sensing and altimetry data.

Kefeng Zhu received the Ph.D. degree in geodetic science from the Ohio State University, OH, USA, in 2015.

His research interests include detection of glacier and water body changes by using polarimetric SAR and optical remote sensing technologies.

Xiao Cheng received the Ph.D. degree in cartography and geography information system from Chinese Academy of Science, Beijing, China, in 2004.

He is currently an associate dean of the College of Global Change and Earth System Science, Beijing Normal University, China. His research interests include icecap, sea ice, and Antarctica ice sheet by using InSAR and ground observation.